Three-dimensional reconstruction of *in vivo* bioluminescent sources based on multispectral imaging

Chaincy Kuo
Olivier Coquoz
Tamara L. Troy
Heng Xu
Brad W. Rice
Caliper Life Sciences
Xenogen Corporation
2061 Challenger Drive
Alameda, California 94501
E-mail: Chaincy.Kuo@caliperls.com

Abstract. A new method is described for obtaining a 3-D reconstruction of a bioluminescent light source distribution inside a living animal subject, from multispectral images of the surface light emission acquired on charge-coupled device (CCD) camera. The method uses the 3-D surface topography of the animal, which is obtained from a structured light illumination technique. The forward model of photon transport is based on the diffusion approximation in homogeneous tissue with a local planar boundary approximation for each mesh element, allowing rapid calculation of the forward Green's function kernel. Absorption and scattering properties of tissue are measured *a priori* as input to the algorithm. By using multispectral images, 3-D reconstructions of luminescent sources can be derived from images acquired from only a single view. As a demonstration, the reconstruction technique is applied to determine the location and brightness of a source embedded in a homogeneous phantom subject in the shape of a mouse. The technique is then evaluated with real mouse models in which calibrated sources are implanted at known locations within living tissue. Finally, reconstructions are demonstrated in a PC3M-luc (prostate tumor line) metastatic tumor model in nude mice. [DOI: 10.1117/1.2717898]

Keywords: luminescence; light propagation in tissues; tomography; diffusion; surface measurements.

Paper 06212R received Aug. 7, 2006; revised manuscript received Dec. 8, 2006; accepted for publication Jan. 11, 2007; published online Apr. 19, 2007.

1 Introduction

Bioluminescent imaging is a noninvasive technique for performing *in vivo* diagnostic studies on animal subjects in the areas of medical research, pathology, and drug discovery and development. Bioluminescence is typically produced by cells that have been transfected with a luminescent reporter such as luciferase, and can be used as a marker to differentiate a specific tissue type (e.g., a tumor), monitor physiological function, or follow the progression of a disease. A wide range of applications has been demonstrated, including areas of oncology,[1,2] infectious disease,[3] inflammation, and metabolic disease.[4,5]

Photons emitted by bioluminescent cells are strongly scattered in the tissue of the subject such that propagation is diffusive in nature.[6] As photons diffuse through tissue, many are absorbed, but a fraction reach the surface of the subject and can be detected. In general, absorption in mammalian tissues is high in the blue-green part of the spectrum ($<$565 nm) and lower in the red and near-infrared (NIR) part of the spectrum (600 to 900 nm).[6] Firefly luciferase has a rather broad emission spectrum ranging from 500 to 700 nm, of which part of the emission spectrum is in the low-absorption region.[7,8]

Since the mean free path for scattering in tissue is short, on the order of $\sim$0.5 mm, photons from deep sources are scattered many times before reaching the surface. Bioluminescent imaging systems effectively record the spatial distribution of these scattered photons emitted from the surface of the subject. However, the most important quantitative information is not directly related to the surface emission, but rather pertains to the bioluminescent source inside the subject. Important parameters are the source brightness (related to the number of light-emitting cells), position, and geometry. Most of the *in vivo* bioluminescent imaging work published to date involves use of single-view 2-D imaging systems,[1–5,7] for which image analysis involves quantifying a light-emitting region of interest (ROI) on the subject surface. While this analysis methodology is simple and provides a good *relative* measure of the internal light source brightness, it does not take into account the source depth and resulting attenuation through tissue necessary to obtain an *absolute* source brightness measurement. Hence, there is interest in developing imaging systems and algorithms that would provide the 3-D tomographic reconstruction of the distribution of photon emission inside the animal from images of radiance measured on the animal surface.

Other groups have reported on tomographic techniques for bioluminescent source location and power, considering tissue optical properties at a single wavelength. Wang, Li, and Jiang discuss issues of uniqueness of the tomographic problem.[9] Gu et al. present an image reconstruction technique for bioluminescent sources using a finite-element approach to compute

Address all correspondence to Chaincy Kuo, Xenogen Corporation, 2061 Challenger Drive, Alameda, CA 94501. Tel.: 510-291-6193; Fax: 510-291-6232; E-mail: chaincy.kuo@caliperls.com

1083-3668/2007/12(2)/024007/12/$25.00 © 2007 SPIE

the forward model in a cubic homogeneous phantom.[10] Cong et al. demonstrate the performance of a finite-element-based bioluminescence tomography algorithm in a cylindrical heterogeneous tissue phantom, which requires *a priori* information on a feasible source distribution.[11] This group expanded their research to simplify and linearize the forward problem by reducing the finite element mesh resolution to large-scale organ structures,[12] and applying the Born theory.[13] Tomographic algorithms for small animal fluorescence imaging in a slab geometry have been developed by Ntziachristos et al.[14–16]

The diffusive nature of light in tissue does pose a challenge for determining unique solutions of the tomographic problem. With bioluminescent imaging, uniqueness can be improved by taking images of the subject from multiple views,[17,18] but this can add to the complexity of instrumentation and the length of imaging time. We propose a simpler and faster method that uses spectral information in the image data to constrain the tomographic solution. Bioluminescent images acquired through a number of bandpass filters were analyzed by Coquoz et al. for single source depth and flux, in which the tissue surface is assumed to be planar.[19] Examining phantom subjects with cylindrically shaped boundaries, Dehghani et al. present reconstructions of bioluminescent sources from multispectral data.[20] Chaudhari et al. discuss their efforts to extract 3-D source distribution from multispectral bioluminescent images of mice by incorporating computed tomography (CT) data to determine the tissue surface topography with finite-element analysis to predict the photon transport in tissue.[21]

In this study, a fast (<1 min) tomographic analysis of single-view multispectral images of bioluminescence is presented. The diffuse luminescence tomographic algorithm (DLIT™) provides estimates on the 3-D location and the photon flux of the sources in the tissue. We show that the kernel matrix can be computed efficiently for complex-shaped objects such as small animals, and is initiated naïve to a source distribution. Unique to our work, the surface topography is measured for each animal subject and is used in the calculation of the kernel matrix.

The intent of this work is to outline the experimental and computational procedures of the diffuse tomography reconstruction technique. Section 2 describes the theory and approximations used in our forward model of photon propagation, including the additional information offered by multispectral images of bioluminescence from animal subjects. The experimental setup for collecting bioluminescent images, as well as the characterization of the surface topography for boundary treatment, is presented in Sec. 3. The tomographic reconstruction technique is validated by analyzing images from a homogeneous phantom mouse in Sec. 4. Results are also presented for luminescent beads implanted in living mice and a metastatic mouse model with luciferase-labeled prostate tumor cells.

2 Theory

2.1 *Photon Diffusion in Tissue*

Light transport in turbid media such as tissue is dominated by scattering and is essentially diffusive in nature.[22] The condition for diffusive transport is that the isotropic scattering coefficient μ_s' be much greater than the absorption coefficient μ_a, so that the change in the photon density is very small between scattering events. In this case, the photon density $\rho(x)$ in a homogeneous medium is governed by the steady-state diffusion equation:

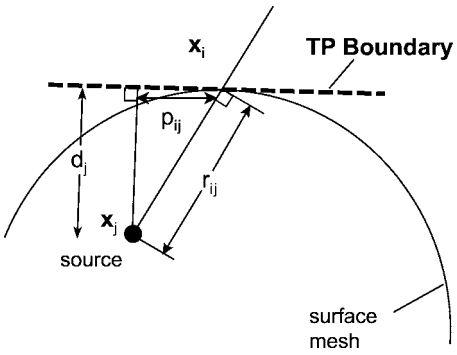

Fig. 1 A schematic diagram illustrating the TP approximation where a plane boundary is drawn tangent to the surface at x_i. The photon density is the solution for a point source at x_j in a semi-infinite slab defined by the plane boundary, subject to the partial current boundary condition. Note that the orientation of the plane boundary is different for each surface element.

$$D\nabla^2\rho(x) - \mu_a c\rho(x) = -U(x), \tag{1}$$

where U is the photon rate density (photons/s/cm^3) and D is the diffusion coefficient,

$$D = \frac{c}{3(\mu_a + \mu_s')}.$$

The source flux $s(x)$ in a volume element δV is given by

$$s(x) = \delta V U(x).$$

The Green's function is the solution to Eq. (1), subject to the boundary condition imposed by the surface of the object. In general, numerical techniques such as Monte Carlo or finite-element modeling (FEM) are required to find a rigorous solution to Eq. (1) with a complex 3-D boundary. However, for the case of a homogeneous object, a tangential planar (TP) approximation can be made to reduce computational cost. In this approximation, shown schematically in Fig. 1, the surface of the object is treated locally as an infinite plane boundary oriented tangentially to the surface at x_i. The orientation of the plane changes for each surface element. This approximation is generally valid when the radius of curvature of the surface is greater than the effective absorption length,

$$1/\mu_{\text{eff}} = 1/[3\mu_a(\mu_a + \mu_s')]^{1/2},$$

a condition that is easily satisfied in most practical cases. A similar technique has been proposed by Ripoll et al.[23]

The Green's function is the following form for a point source in the semi-infinite slab using the partial-current boundary condition[24–27] [see Eq. 2.4.2 in Ref. 27]:

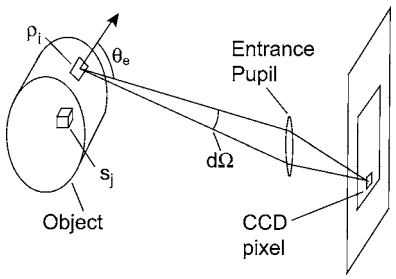

Fig. 2 The object is divided into a solid mesh of voxels, one of which is shown here. Each voxel contains a point light source s_j that contributes to the photon density ρ_i at the surface. The light emission from a surface element passes through the entrance pupil and is recorded in the image. The angle of emission with respect to the surface normal is θ_e. The entrance pupil subtends a small solid angle $d\Omega$.

$$G_{ij}=\frac{1}{2\pi D}\left(\frac{\exp(-\mu_{\text{eff}}r_{ij})}{r_{ij}}-\frac{1}{z_b}\int_0^{\infty}dl \times\exp(-l/z_b)\frac{\exp\{-\mu_{\text{eff}}[(d_j+l)^2+p_{ij}^2]^{1/2}\}}{[(d_j+l)^2+p_{ij}^2]^{1/2}}\right). \quad (2)$$

Here, $r_{ij}=[d_j^2+p_{ij}^2]^{1/2}$, where d_j is the perpendicular distance from the source s_j to the tangent plane, and p_{ij} is the distance along the plane from the surface element at x_i to the perpendicular bisector of length d_j, and

$$z_b=\frac{2D}{c}\frac{1+R_{\text{eff}}}{1-R_{\text{eff}}}.$$

The parameter R_{eff} is the average internal reflection coefficient,[27] depends only on the index of refraction of the tissue underneath a surface element, and is typically in the range of 0.3 to 0.5. A simple analytic approximation (without integral) for Eq. (2) has been developed, in which the extrapolated boundary condition[27] and Eq. (2) with $p_{ij}=0$ are combined by giving the former more weight for large r_{ij}/p_{ij}, and giving the latter more weight for small r_{ij}/p_{ij}. This simplified expression has excellent agreement ($<1\%$ error in photon density predictions) with Eq. (2) for typical source depths and optical parameters, and can be calculated very quickly compared to evaluating the infinite integral.

2.2 *Converting Light Emission to a Photon Density Map*

Photons emitted from the tissue surface are detected by a charge-coupled device (CCD)-based imaging system, as shown in Fig. 2. The surface radiance L (photons/s/cm^2/steradian) is directly related to the photon density ρ (photons/cm^3) just inside the surface element. The exact form of the relationship depends on the model used to describe the transport of photons across the surface boundary, from tissue to air. Derived from the partial-current boundary condition [see Eq. 2.4.6 in Ref. 27], the relationship between L and ρ is

$$L(\theta_e)=\frac{c}{4\pi n^2}T(\theta)\left[1+\frac{3}{2}\frac{1-R_{\text{eff}}}{1+R_{\text{eff}}}\cos\theta\right]\rho, \quad (3)$$

where c is the speed of light, n is the index of refraction of the object medium, T is the transmission coefficient for light exiting the object through the surface element, and θ is the internal emission angle, which is related to the external emission angle θ_e through Snell's law. The imaging system is absolutely calibrated such that electron counts on each CCD pixel can be mapped back onto the surface of the object, producing an absolute value of the surface radiance L from each imaged surface element, as illustrated schematically in Fig. 2. The imaging system collects the light emitted from the surface element at an angle θ_e (measured with respect to the normal to the surface element) into the solid angle $d\Omega$ subtended by the entrance pupil. We can apply Eq. (3) to convert the surface radiance measured at each surface element to values of the photon density directly beneath the surface.

2.3 *Discretizing the Diffusive Transport Problem*

Parameterization of the source intensity solution space is in the form of cubic voxels with a point light source at the center. We assign s_j the value of the strength (or flux in photons/sec) of the point source inside the j'th voxel. A 3-D grid of evenly spaced points defines the basis for source intensities estimated to approximate the actual source distribution. The reconstruction method takes advantage of the linear relationship between the source strength s_j in each voxel and the photon density ρ_i measured at surface elements described by the Green's function G_{ij} [Eq. (2)]. For m observations of photon density comprising column vector $\boldsymbol{\rho}$, and n source points comprising column vector $\mathbf{s}$, $\mathbf{G}$ represents the data kernel matrix of dimension $m\times n$

$$\boldsymbol{\rho}=\mathbf{G}\mathbf{s}. \quad (4)$$

2.3.1 *Wavelength dependence of Green's functions*

In the homogeneous tissue approximation, the inverse problem for source intensities comprised within the boundaries of a closed surface can be nonunique for surface radiance measured using a single wavelength band, particularly for a single-view perspective. In the case of a single point source embedded deep within a semi-infinite tissue slab, the resulting surface radiance could be fit equally well by a point source at the correct depth, or a large array of closely spaced sources at a shallower depth whose intensities are adjusted to match the surface radiance profile. Taking the surface shape into account, as in a mouse, helps to improve the resolution of the solution, but this is not a very strong constraint.

The resolution of the source parameters can be significantly improved using image data measured at different wavelengths. The Green's function in Eq. (2) has a strong wavelength dependence due to the dependence on $\mu_{\text{eff}}(\lambda)$. In the wavelength range of interest ($\lambda\sim 550$ to 700 nm), $\mathbf{G}$ decreases monotonically with wavelength as both $\mu_a(\lambda)$ and $\mu_s'(\lambda)$ [and hence $\mu_{\text{eff}}(\lambda)$] generally decrease with wavelength in this window. If we measure the surface radiance at two or more wavelengths with significantly different $\mathbf{G}$ func-

Table 1 Condition numbers for Green's kernel matrices.

N data	50	100	150	200
Wavelengths in Green's kernel matrix	640 nm	620, 640 nm	600, 620, 640 nm	580, 600, 620, 640 nm
Condition number	1.7×10^7	2.8×10^5	4.2×10^4	1.2×10^4

tions, and the wavelength dependence of $\mathbf{G}$ and $\mathbf{s}$ is known, then resolution of the solution to Eq. (4) is enhanced. In the semi-infinite slab example stated before, the incorrect shallow-source solution would not be allowed because this solution cannot fit the data for multiple wavelengths simultaneously.

Equation (4) can be rewritten to include multiple wavelengths as

$$\begin{bmatrix} \boldsymbol{\rho}(\lambda_1) \\ \vdots \\ \boldsymbol{\rho}(\lambda_k) \end{bmatrix} = \begin{bmatrix} \eta(\lambda_1)\mathbf{G}(\lambda_1) \\ \vdots \\ \eta(\lambda_k)\mathbf{G}(\lambda_k) \end{bmatrix} [\mathbf{s}]$$

$$\tilde{\boldsymbol{\rho}} = \tilde{\mathbf{G}}\mathbf{s}, \tag{5}$$

where the wavelength dependence in elements of $\mathbf{G}(\lambda_k)$ comes into the terms $D(\lambda_k)$, $\mu_{\text{eff}}(\lambda_k)$, and $z_b(\lambda_k)$ of Eq. (2). $\eta(\lambda_k)$ is the relative fraction at which the wavelength λ_k contributes in the source emission spectrum, and is given by

$$\eta(\lambda_k) = \frac{\int_{\lambda_k^{\text{lo}}}^{\lambda_k^{\text{up}}} \xi(\lambda) d\lambda}{\int_0^{\infty} \xi(\lambda) d\lambda}, \tag{6}$$

where λ_k^{lo} and λ_k^{up} denote the lower and upper limits of the bandpass filter centered on wavelength λ_k, and $\xi(\lambda)$ is the light source emission spectrum. $\eta(\lambda_k)$ is introduced so that source flux unit (photons/second) is integrated over all wavelengths.

To illustrate improved resolution in a single-view system afforded by adding spectral information, singular value decomposition was performed for Green's function kernel matrices for a source-detection geometry in a 2-D tissue slab oriented in the x-z plane. The 1×1-cm slab was pixelized into a 4×4 grid, with the pixel centers denoting source locations. Detection points were evenly spaced across the top boundary to emulate a single-view tomographic geometry. Green's kernel matrices were computed for a number of wavelength combinations using *in vivo* mouse muscle optical properties (the experimental measurement is addressed in Sec. 4.1) and the firefly luciferase emission spectrum measured at 37 °C. For each wavelength, 50 detection points were used. Singular value decomposition was performed on each of the kernel matrices representing the wavelength combinations, and the singular values were used to compute the condition number of the Green's kernel matrices. Table 1 shows that for the discretized parameterization of source locations in tissue and detection points described before, the poor pose of the Green's kernel matrix is improved, demonstrated by decreasing condition number with additional wavelength information.

2.4 *Optimization for Source Estimation*

The source intensities are determined by finding

$$\min\|\mathbf{W}(\tilde{\boldsymbol{\rho}} - \tilde{\mathbf{G}}\mathbf{s})\|_2^2 \text{ subject to } \mathbf{s} \geqslant 0, \tag{7}$$

where $\mathbf{W}$ is a diagonal matrix of weights of dimension m, and $\|\cdot\|_2^2$ denotes Euclidean length squared. A constrained optimization algorithm[28] is implemented to solve Eq. (5), to guarantee physical non-negative values for the estimated source intensities $\hat{\mathbf{s}}$. The algorithm requires that $m \geqslant n$, to ensure that the inverse problem is not underdetermined. The weight W_{ii} is assigned to be the inverse of the instrument noise and statistical noise associated with the photon detection at surface element i wavelength k. Assuming Poisson distributed noise,

$$W_{ii} \propto 1/\sqrt{N_{\text{counts}} + N_{\text{rd}}^2},$$

where N_{counts} is the number of photon counts per pixel and N_{rd} is the read noise of the camera system. The inverse weights, initially in units of counts, are converted to radiance units (photons/second/cm^2/steradian), and then to photon density units (photons/mm^3) as described in Sec. 2.2.

While high resolution localization is sought, a densely gridded source parametrization contributes to ill-conditioning of the inverse problem. To maintain high rank in the linear problem, the source parameterization is initially defined to be coarse, and an iterative locally adaptive gridding scheme is adopted. In each refinement step, solution voxels below a critical threshold (0.1% of the estimated source maximum) are suppressed in the source parameterization, and solution regions of high intensities are refined by decreasing the grid spacing by one half. The number of source parameters varies between refinements steps. Therefore, we use

$$\chi_v^2 = \frac{1}{m-n}\|\mathbf{W}(\tilde{\boldsymbol{\rho}} - \tilde{\mathbf{G}}\hat{\mathbf{s}})\|_2^2,$$

called the reduced χ^2, as the figure of merit to compare the goodness of fit between one refinement step to the next. Adaptively refined meshes have been utilized in fluorescent tomographic studies as well.[29]

After estimating source locations and intensities by the diffuse luminescence tomographic analysis, solutions can be characterized by calculating the total flux

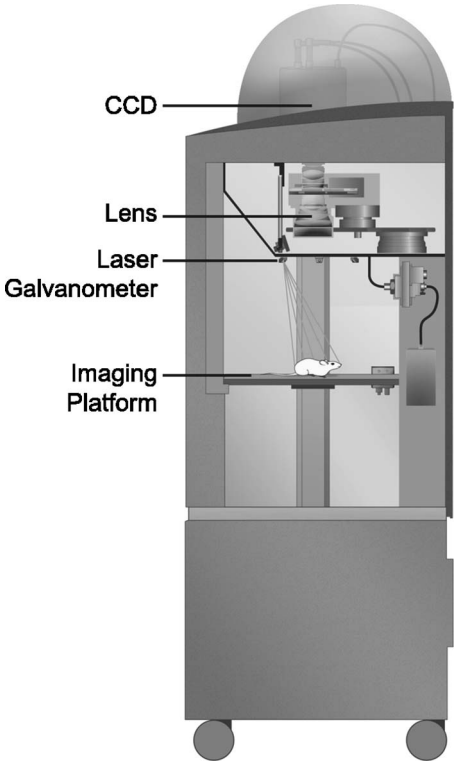

Fig. 3 A schematic diagram of a cross sectional view of the IVIS 200 Imaging System. The laser galvanometer projects lines onto the animal for the structured light imaging feature.

$$s_{\text{tot}} = \sum_j \hat{s}_j,$$

and the center of mass of the estimated source distribution

$$\vec{r}_{\text{cm}} = \sum_j \vec{r}_j \hat{s}_j / s_{\text{tot}}.$$

Source depths are estimated by taking the distance from the source center of mass to the surface, in the z direction.

3 Experimental Setup

3.1 *Description of the Imaging System*

The images in this study were obtained on an IVIS® 200 Imaging System (Xenogen Corporation), as shown in Fig. 3. The system uses a back-thinned integrating CCD with high quantum efficiency over the spectral range of 400 to 950 nm, which covers the tissue transmission window of 600 to 950 nm. Cooling the camera to less than −90 °C reduces the dark current to <100 electrons/s/cm^2 and the associated noise to near-negligible levels.[7] Imaging is performed with a high-sensitivity f/1 lens. The viewing platform for this instrument has mobility along the optical axis, where the fields of view can range from 3.9 to 26 cm. The imaging system is absolutely calibrated to convert electron counts measured on the CCD, to surface radiance emitted at the imaging subject surface in units of photons/sec/cm^2/steradian. Conversion coefficients are calibrated for each f-stop and field of view. Multispectral capability in this instrument is possible through six 20-nm-wide bandpass filters spaced every 20 nm from 560 to 660 nm, which are set in the 24-position filter wheel. The instrument is equipped with a laser scanner that projects line patterns onto the animal, and this provides images from which the surface topography of the subject can be rendered.

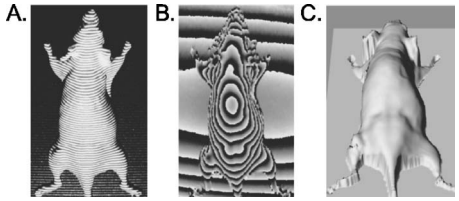

Fig. 4 Structured light analysis to determine surface topography: (a) single-view structured light image; (b) phase shift determined from fast Fourier transform (FFT), and (c) 3-D surface from phase unwrapping.

3.2 *Structured Light Determination of Surface Topography*

The surface topography is necessary to define the boundary condition of diffuse photon propagation at the tissue-air boundary. To determine the surface topography of the subject animal, a structured light technique has been implemented. Using a computer-controlled laser galvanometer, a series of parallel lines are projected down on the subject at a 20.6° angle. A structured light image of the illuminated subject is then acquired with the CCD, as shown in Fig. 4(a). The animal's height can be determined by analyzing the bending or displacement of the lines as they pass over the animal. To determine surface topography from the structured light image, we utilize a two-step method that involves a 2-D Fourier transform[30] combined with a phase-unwrapping algorithm.[31]

In Fourier space, a prominent peak near the reference frequency is broadened, due to the shift in phase of the lines when passing over the animal subject. The reference frequency is the line frequency at the center of the field of view on a flat surface. The constant and low-order terms, due to the positivity of image intensities and brightness of the animal relative to the black stage, also have significant amplitude in Fourier space. To compute the phase shifts relative to the reference frequency, the low-order terms and high-order harmonic terms must be filtered out using a bandpass filter. A cosine-tapered bandpass filter is applied to the Fourier spectrum to filter out the low-order terms, and high-order harmonics. The broadened peak selected out by the Fourier bandpass filter is then shifted to the Fourier space origin, and the inverse Fourier transform is applied to give $s_F(x,y) = b(x,y)\exp[i\varphi(x,y)]$, where the index F denotes the filtered image.

The phase

$$\varphi(x,y) = \tan^{-1}\left\{\frac{\Im[s_F(x,y)]}{\Re[s_F(x,y)]}\right\}$$

at each pixel location can then be calculated in the range $\varphi(x,y) = (-2\pi, 2\pi]$, as shown in Fig. 4(b). These phase values must be unwrapped across the whole image to obtain the absolute phase. The unwrapping of phase across an image involves integration of phase values over a pathway through

the image. As residues often occur as a result of image noise, a well-defined path avoiding residues is essential to correctly determining the surface heights. We have employed a quality-guided path phase-unwrapping technique, which first assigns a phase image subsection quality, and then directs the phase-unwrapping path based on the phase image subsection quality. The quality measure utilized here is the phase-derivative variance.[31] Once the absolute phase is calculated for the image, the height can be determined approximately by the relation

$$h(x,y) \approx \frac{L\phi(x,y)}{2\pi f_0 D}, \tag{8}$$

where $\phi(x,y)$ is the absolute phase of the animal subject. The exact expression for Eq. (8) requires some correction terms due to the finite distance between the lens/projector and the animal subject.

The final unwrapped surface topography is shown in Fig. 4(c). The line spacing and unwrapping algorithms give a surface accuracy of ~0.5 mm for smooth surfaces. Only the top surface of the animal facing the imaging system is rendered correctly with this technique. To construct a closed surface, the edge of the mouse surface is cropped vertically to the imaging platform and is closed horizontally across the bottom.

4 Experimental Results

4.1 *Phantom Mouse Experiment*

To assess the validity of the IVIS200 instrumentation and DLIT reconstruction algorithm, tests have been performed with a mouse-shaped homogeneous tissue phantom. To produce this phantom, a nude mouse was sacrificed, frozen, and the surface topography was scanned by a commercial machine vision scanner. The result was a high-resolution 3-D computer model from which a rubber mold was made. The rubber mold was then used to cast a phantom mouse with dimensions of approximately 3 to 4 cm in width (side to side), 9 cm in length (nose to feet), and 2.2 cm in height (dorsal to ventral). The composition of the phantom is similar to that described by Vernon et al.,[32] using a polyester resin as the host material, TiO_2 for scattering, and Disperse Red for absorption. The optical properties were independently measured from a rectangular slab that was made from the same batch of material as the plastic mouse. The absorption μ_a and reduced scattering μ_s' coefficients were measured using a double integrating sphere apparatus along with the inverse adding doubling method.[33,34] Curve fits to the intensity profile using a slab diffusion model with the partial current boundary condition were used as an alternate method to confirm the optical property values.[7,27] Two 200-μm fiber optics coupled to green LEDs were embedded into the phantom at two different known locations, labeled source A and source B. Depth measurements are from the fiber tip to the phantom surface along the z direction with respect to when the phantom is in a prone or supine position. Before insertion, the power emitted from each fiber optic was measured with a Newport Optical Power Meter (model 840), and converted to units of photons/sec for the wavelength of the spectral peak (567 nm). LED spectral profiles emitted from the fibers were characterized in an Ocean Optics USB2000 Fiber Optic Spectrometer. The profiles of the optical properties and spectra are shown in Fig. 5. Each LED is independently controlled with a switch to allow for a combination of light-emitting source configurations. A schematic drawing of the phantom mouse is shown in Fig. 6. An image sequence for tomographic analysis involves acquiring a photographic image (grayscale, illuminated reference image), a structured light image, and several luminescent images through different filters. These images were acquired for the mouse-shaped tissue phantom with the different source configurations and phantom positions. Luminescent data were acquired through four 20-nm-wide bandpass filters centered

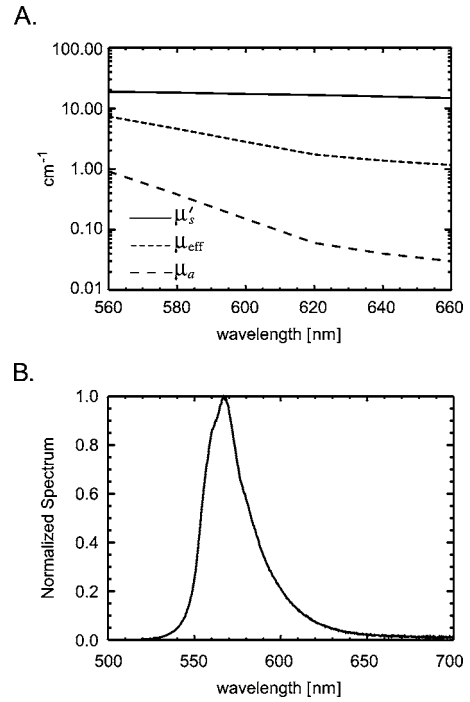

Fig. 5 (a) Optical properties of the mouse-shaped tissue phantom. The dotted line is μ_s', the dashed line is μ_a, and the solid line is μ_{eff}. (b) The combined normalized wavelength spectrum of the two green LEDs coupled to fiber optics, which are embedded in the phantom.

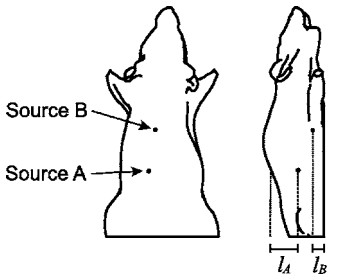

Fig. 6 Schematic drawing of the mouse tissue phantom. The phantom mouse is made of polymer resin with added scatterer and absorbing dye to simulate optical properties of mouse muscle. Two LEDs are coupled to embedded fiber optics ($l_{\max}$=570 nm), whose tips are labeled as source A and source B in the drawing. The distance of source A to the dorsal side of the phantom is l_A=9.4±0.5 mm, and the distance of source B to the ventral side of the phantom is l_B =4.1±0.5 mm.

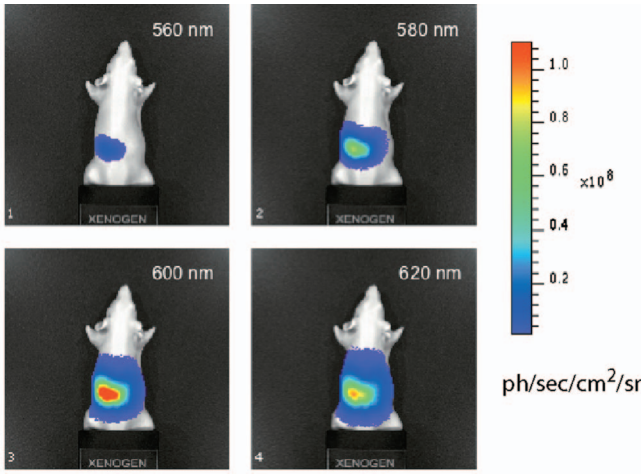

Fig. 7 Surface radiance images of the phantom mouse dorsal side with embedded fiber optic source A measured through 20-nm-wide bandpass filters, centered at 560, 580, 600, and 620 nm.

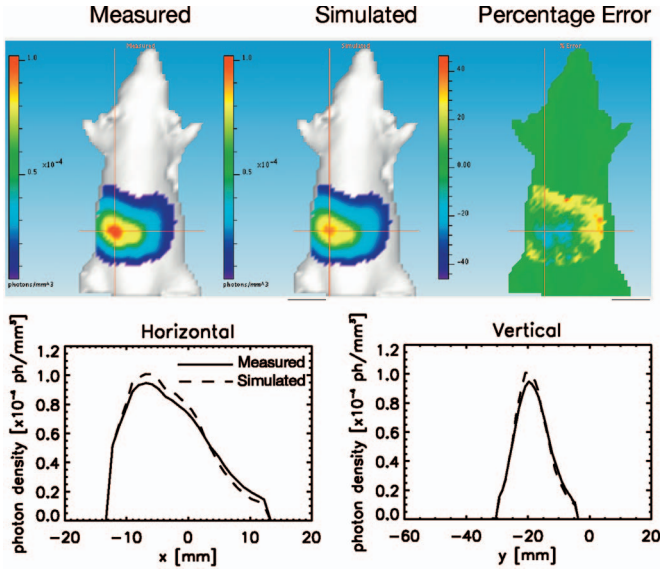

Fig. 9 Top row: comparison of the measured (left) and simulated (middle), and percentage error (right) images of photon density at 620 nm from the dorsal source A reconstruction of Table 3. Profiles on the bottom row show the photon density fit of the simulated photon density (dashed) to the measured photon density (solid) for a horizontal and vertical profile through mouse phantom, as indicated by the red cursor lines on the top row.

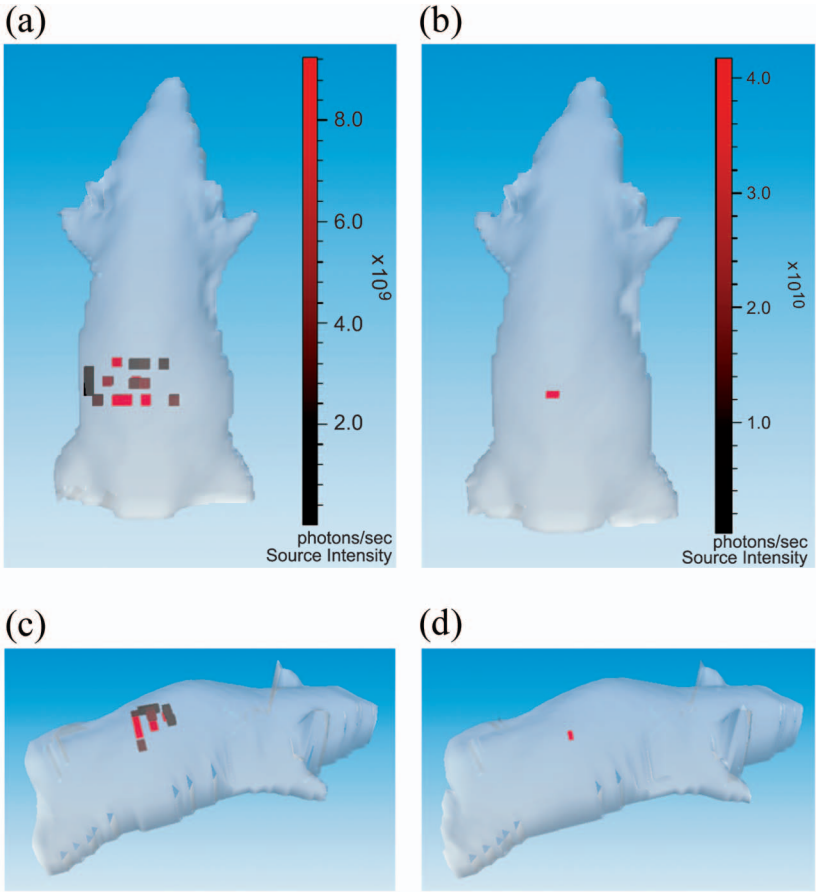

Fig. 8 Diffuse luminescent tomographic estimates of LED source A for (a) single wavelength data at 620-nm filter, and (b) dual wavelength data at 580 and 620 nm. The lateral views of each case are shown in (c) and (d), respectively. Source voxels are displayed on a red-black color scale in units of photons/sec. Voxels <2% of the max are suppressed.

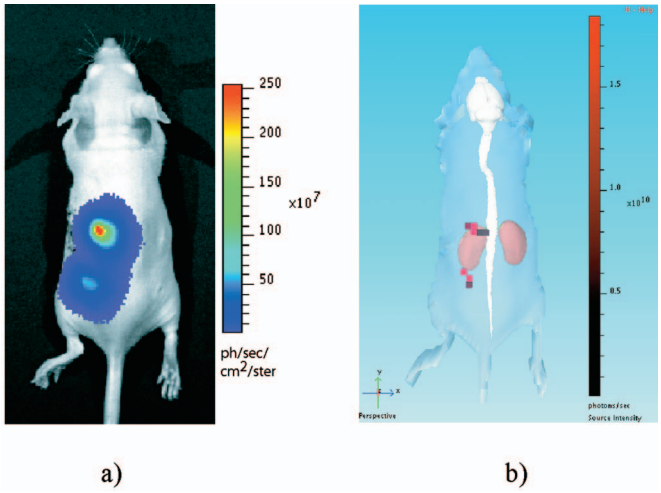

Fig. 10 (a) Unfiltered image of luminescent beads implanted next to the left kidney. (b) Source reconstruction and organ atlas of mouse kidneys, brain, and spinal column in the surface mesh. Sources above 5% of the maximum intensity are displayed as voxels in red-black fade color.

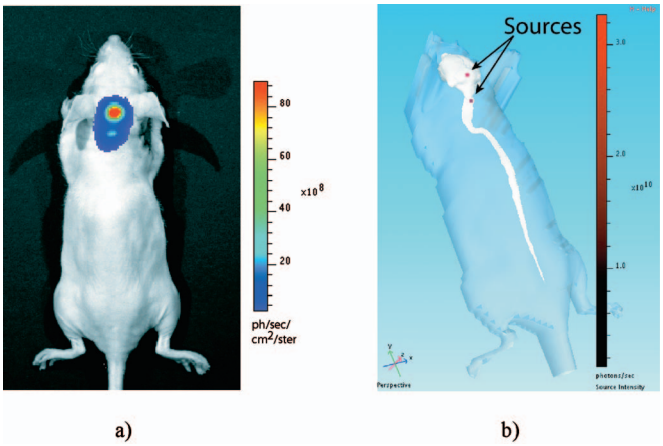

Fig. 11 (a) Unfiltered image of two luminescent beads implanted between the trapezius muscles. (b) Source reconstruction of luminescent beads implanted in-between the trapezius muscles. Sources above 2% of the maximum intensity are displayed as voxels in red-black fade color, and the mouse reference atlas organ brain and spinal column are displayed within the surface mesh.

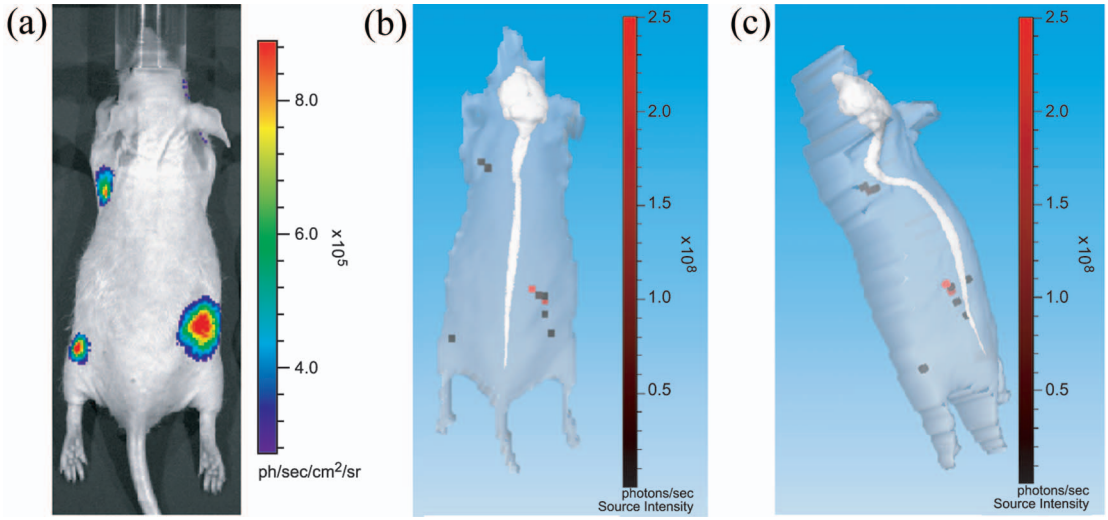

Fig. 12 (a) Dorsal view of unfiltered image of mouse injected with PC-3M-luc cells, 29 days postinjection. (b) and (c) Top and perspective view of source reconstruction with atlas brain and spinal column are displayed. Voxels <1% of the maximum are suppressed.

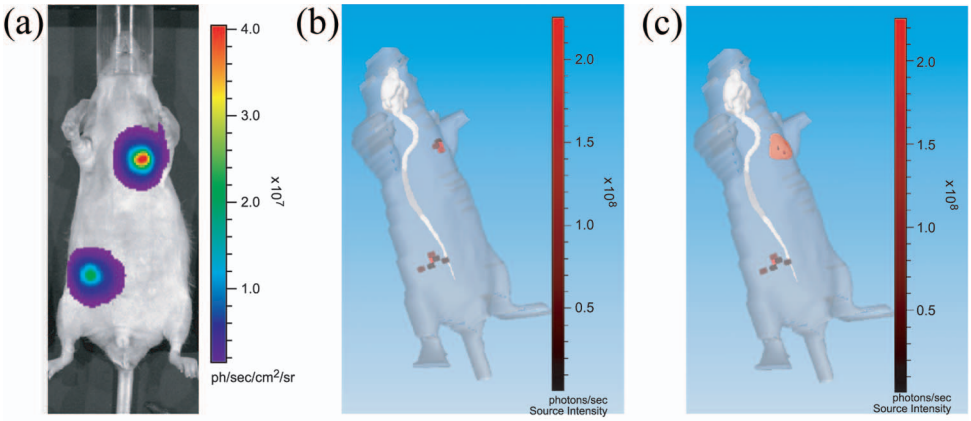

Fig. 13 (a) Ventral view of unfiltered image of mouse injected with PC-3M-luc cells, 29 days postinjection. (b) Source reconstruction with atlas brain and spinal column are displayed. Voxels <5% of the maximum are suppressed. (c) is the same as (b), except the heart atlas organ is displayed as well.

Table 2 Tomographic estimates of the flux for Figs. 8(a) and 8(b).

	Source flux ($\times 10^{10}$ photons/sec)	Relative error
Physical	7.7±0.4	—
620 nm	4.1	48%
580 nm+620 nm	7.5	3%

on 560, 580, 600, and 620 nm. The phantom mouse was imaged in two positions: 1. with the dorsal side facing the camera, and 2. with the ventral side facing the camera. Three source configurations were imaged: source A, source B, and source A and B. Raw images of surface radiance for case 1, source A are shown in Fig. 7.

Structured light analysis was performed to render the portion of the phantom surface visible to the camera lens. Data acquired through each filter were selected by setting a dynamic range value for each filter image. The dynamic range is defined here to be the luminescent image maximum signal divided by an *a priori* threshold signal, below which is considered to be due to camera noise or animal background.[35] The signal above the threshold given by the dynamic range is converted to photon density on the surface vertices, as described by Eq. (3). A fixed number of surface data elements for each filtered image are chosen, to equalize data weighting between the bandpass filtered data.

4.1.1 *Single-wavelength versus multiple-wavelength data*

The resolution gained by incorporating wavelength-dependent Greens functions is demonstrated by testing combinations of filtered data used in the source estimation. In Fig. 8(a), the source intensity distribution when source A was powered on was determined by data from a single wavelength filter centered on 620 nm. 400 data points were included in the data vector. The broad source distribution reveals the low resolvability afforded by the model used for single wavelength data. In an inversion including data from the 580-nm centered wavelength band, where the optical properties are distinctly different from those at 620 nm, the source localization becomes much tighter, as seen in Fig. 8(b). The data vector consisted of 200 data points from each filtered dataset, for a total of 400 data points. The source intensity is also better resolved when using multiple spectra in the data, as shown in Table 2.

4.1.2 *Four wavelength filtered data*

Incorporating as much information as possible, image data of the phantom mouse from the four bandpass filters centered at 560, 580, 600, and 620 nm were used in the inversion, and results are tabulated in Table 3 for different source and viewing configurations. For each filtered image, 200 data points were selected, giving a total of 800 data points. The source estimations were tightly localized, similar to the distribution in Figs. 8(b) and 8(d). Accuracy in depth is within a millimeter, and intensities were estimated within ~19% relative error for the LED sources. Voxel sizes were typically refined to side length of 1 mm.

The measured photon density at the visible surface is simulated well by the photon density forward modeled from the source estimate. The fit for 620-nm data is shown in Fig. 9, where the photon density on the surface is displayed along the top row as a pseudocolor map overlaying the surface rendered in shaded white. Measured photon density data used in the fit lie within the pseudocolor map area shown on the left of the top row in Fig. 9, the simulated photon density overlaying the surface is shown in the middle, and the relative error map is shown on the right. Measured photon density values below the level of image noise were not used in the fit and were located at the surface area, which appears white in the left and middle maps. Line profiles drawn through the photon density

Table 3 DLIT estimates of fiber optic sources in the mouse-shaped tissue phantom. Data included luminescent images collected through the 560-, 580-, 600-, and 620-nm filters.

		Source A		Source B	
Experiment	Measurement	Depth [mm]	Flux (photons/sec)	Depth [mm]	Flux (photons/sec)
Dorsal	Physical	9.4±0.5	7.7±0.4 $\times 10^{10}$	17.6±0.5	6.3±0.3 $\times 10^{10}$
Source A on	Tomographic	9.8	7.8×10^{10}	—	—
Source B on	Tomographic	—	—	16.4	5.1×10^{10}
Ventral	Physical	9.9±0.5	7.7±0.4 $\times 10^{10}$	4.1±0.5	6.3±0.3 $\times 10^{10}$
Source A on	Tomographic	10.3	7.1×10^{10}	—	—
Source B on	Tomographic	—	—	4.5	7.9×10^{10}
Source A and B on	Tomographic	10.3	7.5×10^{10}	4.6	7.6×10^{10}

maps are plotted and compared, displayed on the bottom row of Fig. 9.

4.2 *In Vivo Studies*

In vivo tissue is optically heterogeneous, and blood oxygenation levels cast additional fluctuations into the optical properties of the tissue. To assess the use of the homogeneous tissue approximation in the DLIT algorithm within heterogeneous tissue, we performed experiments with calibrated luminescent sources *in vivo*, where source locations and strengths are known. Tomographic results are also presented from metastasis model experiments in which tumor cells labeled with firefly luciferase are introduced into *in vivo* subjects.

4.2.1 *Calibrated luminescent sources*

To benchmark the performance of the homogeneous tissue model adopted by the reconstruction algorithm, tritium-filled glass beads with interior phosphor coating were used as calibrated luminescent sources *in vivo*.[5] Tritium is a β-emitter, and the absorption of the β by the phosphor induces photon emission with invariable power over the time scales of the experiments. The glass beads are 1 mm in diameter and 3 mm in length. Luminescent bead power was measured by placing the beads on black felt as an absorbing background and imaging them in the IVIS 200 Imaging System. Radiance measurements were integrated over the bead interior surface area and 2π steradians to convert to absolute flux. The bead spectrum was characterized on the Ocean Optics spectrometer.

In each of the following experiments, a 25- to 30-g male nude mouse was anesthetized with a 4:1 concentration of ketamine and xylazine at a 15 μl per 10-g body weight dose rate by interperitoneal injection. A 100-min period state of unconsciousness is expected. Once anesthesia was determined to have taken effect, luminescent beads were surgically implanted in specific locations. After implantation, surgical wounds were sutured and the animal was imaged in the camera system. The sutured incisions were located so that surface radiance from the beads could be imaged through undamaged skin. The animal was imaged in the camera using five bandpass filters centered at 560, 580, 600, 620, and 640 nm. Before consciousness could be regained, the animals were euthanized using compressed carbon dioxide. Post-expiration, the bead locations were surgically determined and intact locations were gauged with calipers. *In vivo* optical properties for muscle and the normalized spectrum of the luminescent beads were used in the DLIT reconstruction. *In vivo* optical properties of a number of mouse organs were measured with the method described in Bevilacqua et al.[36]

Luminescent beads were implanted in contact with the left kidney of a male nude mouse, with one at the cranial end and another at the caudal end of the kidney. The DLIT solution using data from the 560-, 580-, and 640-nm bandpass filters produced the lowest reduced χ^2. The physical and tomographic measurements are outlined in Table 4. Source depths and intensities are very well estimated, with less than 6% error in source intensity and 0.5-mm error in depth. Figure 10(a) shows the unfiltered raw data image. An anatomical mouse reference atlas showing brain, spinal column, and kidneys is displayed with the DLIT estimation inside the surface mesh in Fig. 10(b). The sources estimated by DLIT are located at the cranial and caudal end of the reference atlas kidneys, suggesting tomographic agreement with the implantation sites.

Table 4 DLIT estimates of luminescent beads implantation near the left kidney, dorsal view.

	Cranial bead		Caudal bead	
Measurement	Depth (mm)	Flux (ph/sec)	Depth (mm)	Flux (ph/sec)
Physical	3.4±0.5	3.5×10^{10}	5.7±0.5	3.5×10^{10}
DLIT	3.2	3.7×10^{10}	5.9	3.8×10^{10}

In a second experiment, two luminescent beads were implanted in close proximity, between the right and left trapezius muscles of a male nude mouse. One bead was placed cranially, and the second was placed close to the first thoracic vertebra. Physical and tomographic measurements are summarized in Table 5 and Fig. 11. For these shallow sources, the center of mass depths were estimated with submillimeter accuracy, and the sources are well localized. The distance between the estimated source center of masses was 7.1 mm. Again, the source intensity estimation is in very good agreement with the measured power of the beads.

4.2.2 *Tumor models*

Monitoring metastatic disease in animals with DLIT was investigated by introducing 2×10^6 tumorigenic PC-3M-luc cells to a 30-gram male nude mouse by injection into the left ventricle of the heart. The cells were given time to colonize *in vivo* and develop into metastases. On day 29 postinjection of the PC-3M-luc cells, the animal was administered a dose of 15 μl per 10-g body weight of luciferin by intraperitoneal injection. The luciferin kinetic profiles have been measured for this cell line and show that luciferin is taken up for approximately 10 min postinjection, and a plateau is sustained for a 25- to 30-min period postinjection. Anesthesia was induced with an isofluorane gas mixture. The animal was imaged dorsally in the camera 10 min after injection of luciferin to guarantee sufficient signal. The ventral view was imaged 17 min after the initial luciferin injection. Four bandpass filtered images were acquired at 580-, 600-, 620-, and 640-nm center frequencies, and the bandpass filtered image sequence was preceded and followed by an image acquired without a bandpass filter to evaluate the stability of luciferin kinetics during imaging. The imaging acquisition time of each filtered sequence totaled 3 min.

Table 5 DLIT estimates of luminescent beads implanted between the trapezius muscles, dorsal view.

	Cranial bead		Cervical bead	
Measurement	Depth (mm)	Flux (ph/sec)	Depth (mm)	Flux (ph/sec)
Physical	1.5±0.5	3.5×10^{10}	2.3±0.5	3.5×10^{10}
DLIT	1.3	4.0×10^{10}	3.0	3.0×10^{10}

Table 6 DLIT estimates of PC-3M-luc lesions, dorsal and ventral views.

	Left femur		Left cardiac		Peritoneal cavity	
Measurement	Depth (mm)	Flux (ph/sec)	Depth (mm)	Flux (ph/sec)	Depth (mm)	Flux (ph/sec)
DLIT dorsal	1.9	1.0×10^{7}	6.2	3.6×10^{7}	10.1	3.9×10^{8}
DLIT ventral	—	—	2.3	3.6×10^{8}	3.7	3.9×10^{8}

The data were analyzed with DLIT using optical properties of *in vivo* muscle and the spectrum of firefly luciferase. The dorsal view image data acquired in the absence of a bandpass filter at the start of imaging were shown in Fig. 12(a), and the DLIT source estimation results are shown in Fig. 12(b). The same are shown for the ventral view in Fig. 13. Source depth and intensity estimates are reported in Table 6. From the dorsal view data, sources in the left femur and in the right peritoneal cavity are estimated by the tomographic algorithm. In the raw data, a bright spot radiating from the left forelimb skin is observed. On the ventral view, a source in the cardiac region is estimated by DLIT, in addition to the source in the right peritoneal cavity. Signal from the femur is not detected on the ventral view raw data image.

From inspection of the analyzed dorsal data, we associate the source estimated in the animal's left forelimb with light emanating from the cardiac region, as seen from the ventral side of the animal in Fig. 13(a). It is conceivable that light from the cardiac source propagated and leaked out toward the skin under the left forelimb. The limited perspective for this source on the dorsal side results in tomographic localization of the source next to the left forelimb and estimates the flux to be ten-fold lower compared to the ventral side estimate. In Fig. 13(c), the mouse heart atlas organ overlay indicates that the reconstructed source is in the cardiac region. We interpret that some PC-3M-luc cells introduced to the mouse via intracardiac remained colonized there.

Despite the optically heterogeneous intestinal organs in which the peritoneal source may be embedded, the estimated source intensity is in agreement between the dorsal and ventral views. The location of the peritoneal source is estimated to be 3.8 mm deep from the ventral surface and 10.1 mm from the dorsal surface. The depths from the opposing surfaces add to ~14 mm. Measurements of the thickness of this mouse from lateral view images gives ~14 to 15 mm at the approximate location of the source, and suggests colocalization by DLIT from the dorsal and ventral sides.

5 Discussion

A new technique called diffuse luminescence imaging tomography (DLIT) has been developed for obtaining a 3-D reconstruction of the bioluminescent source distribution inside a complex object such as an animal subject. The technique is based on the analysis of multiple images of the light emission from a single perspective of the object acquired through a number of bandpass filters. The image data are combined with an independent measurement of the surface topography to produce a high-resolution map of the photon density at the surface. The advantage of using imaging to characterize the surface light emission is that it allows the complete characterization of subjects having complex surfaces, such as a mouse. This technique can yield in real time detailed information about the strength and position of the internal light sources.

The reconstruction algorithm consists of finding an approximate solution to a system of linear equations that relate the source strength at each point inside the object to the photon density at the surface. We have presented a simple form for the Green's function, called the tangential plane (TP) approximation, based on the diffusion model for photon transport. The TP approximation takes into account the effective reflectivity of the surface and can be expressed in a very computationally efficient manner. Light sources are estimated by minimizing forward modeled photon density misfit to the data using a non-negative least-squares algorithm.

As a demonstration of the DLIT technique, we have determined the 3-D source distribution from measured single-perspective, multiple-bandpass spectra images of a phantom mouse and live mice with one or two calibrated internal light sources. In these test cases, the reconstruction technique was able to locate the multiple sources with a depth accuracy of <1 mm, and 1 to 20% relative error in intensity, for sources inside the complex object surface. An *in vivo* mouse tumor model experiment was conducted in which the mouse was imaged viewing its dorsal and ventral side. A tumor producing prominent signal on both sides was identified at depth in the peritoneal cavity by DLIT, and the light intensity estimates from the dorsal and ventral side were in agreement. Source strength and location were retrieved with high accuracy in the *in vivo* bead studies for a number of implantation sites, and we find the agreement in source strength of the deep peritoneal tumor source to be encouraging. The reconstruction algorithm is very fast, requiring about a minute on a 3.4-GHz PC for iterations on 800 data elements and adaptively refined solution space of up to ~200 elements.

Our results to date suggest that the homogeneous approximation appropriately determines light source location and intensity for sources in a number of regions in the living mouse. However, for photon propagating through more pronounced heterogeneous paths, through the liver and lungs, for example, the tomographic model may require a more sophisticated description of photon transport and *in vivo* tissue optical property measurements for more accurate source estimations in living animal models. Methods to extend the DLIT algorithm to include heterogeneous tissue properties are facilitated by the digital mouse atlas and are under investigation.

The tomographic results presented here are in the context of a single-view imaging system, which has the advantage of high throughput, but the disadvantage in that not all sides of

the mouse can be imaged simultaneously. The DLIT algorithm can be applied equally well to multiview optical imaging systems, and this will be discussed in a future publication.

Acknowledgments

The authors would like to acknowledge John Hunter for designing the tumor model experiments, and Haroon Ahsan and Joan Dusich for their technical support with the animal experiments. We would like to extend our gratitude to Dan Stearns for his valuable contributions to the foundation of this work.

References

1. C. H. Contag, D. Jenkins, P. R. Contag, and R. S. Negrin, "Use of reporter genes for optical measurements of neoplastic disease *in vivo*," *Neoplasia* **2**, 41–52 (2000).
2. A. Rehemtulla, L. D. Stegman, S. J. Cardozo, S. Gupta, D. E. Hall, C. H. Contag, and B. D. Ross, "Rapid and quantitative assessment of cancer treatment response using *in vivo* bioluminescence imaging," *Neoplasia* **2**, 491–495 (2000).
3. K. P. Francis, J. Yu, C. Bellinger-Kawahara, D. Joh, M. J. Hawkinson, G. Xiao, T. F. Purchio, M. G. Caparon, M. Lipsitch, and P. R. Contag, "Visualizing pneumococcal infections in the lungs of live mice using bioluminescent streptococcus pneumoniae transformed with a novel gram-positive lux transposon," *Infect. Immun.* **69**, 3350–3358 (2001).
4. S. Gross and D. Piwnica-Worms, "Real-time imaging of ligand-induced IKK activation in intact cells and in living mice," *Nat. Methods* **2**, 607–614 (2005).
5. M. Fowler, J. Virostko, Z. Chen, G. Poffenberger, A. Radhika, M. Brissova, M. Shiota, W. E. Nicholson, Y. Shi, B. Hirshberg, D. M. Harlan, E. D. Jansen, and A. C. Powers, "Assessment of pancreatic islet mass after islet transplantation using *in vivo* bioluminescence imaging," *Transplantation* **79**, 768–776 (2005).
6. V. Tuchin, *Tissue Optics*, SPIE Press, Bellingham, WA (2000).
7. B. W. Rice, M. D. Cable, and M. B. Nelson, "*In vivo* imaging of light emitting probes," *J. Biomed. Opt.* **6**(4), 432–440 (2001).
8. H. Zhao, T. C. Doyle, O. Coquoz, F. Kalish, B. W. Rice, and C. H. Contag, "Emission spectra of bioluminescent reporters and interaction with mammalian tissue determine sensitivity of detection *in vivo*," *J. Biomed. Opt.* **10**(4), 41210 (2005).
9. G. Wang, Y. Li, and M. Jiang, "Uniqueness theorems in bioluminescence tomography," *Med. Phys.* **31**, 2289–2299 (2004).
10. X. J. Gu, Q. Z. Zhang, L. Larcom, and H. B. Jiang, "Three-dimensional bioluminescence tomography with model-based reconstruction," *Opt. Express* **12**, 3996–4000 (2004).
11. W. X. Cong, G. Wang, D. Kumar, Y. Liu, M. Jiang, L. H. Wang, E. A. Hoffman, G. McLennan, P. B. McCray, J. Zabner, and A. Cong, "A practical reconstruction method for bioluminescence tomography," *Opt. Express* **13**, 6756–6771 (2005).
12. W. X. Cong and G. Wang, "Boundary integral method for bioluminescence tomography," *J. Biomed. Opt.* **11**(2), 020503 (2006).
13. W. X. Cong, K. Durairaj, L. V. Wang, and G. Wang, "A Born-type approximation method for bioluminescence tomography," *Med. Phys.* **33**, 679–686 (2006).
14. V. Ntziachristos and R. Weissleder, "Charge-coupled-device based scanner for tomography of fluorescent near-infrared probes in turbid media," *Med. Phys.* **29**, 803–809 (2002).
15. V. Ntziachristos, C. Tung, C. Bremer, and R. Weissleder, "Fluorescence molecular tomography resolves protease activity *in vivo*," *Nat. Med.* **8**, 757–760 (2002).
16. V. Ntziachristos and R. Weissleder, "Experimental three-dimensional fluorescence reconstruction of diffuse media by use of a normalized Born approximation," *Opt. Lett.* **26**, 893–895 (2001).
17. C. Kuo, H. Ahsan, J. Hunter, T. Troy, H. Xu, N. Zhang, and B. Rice, "*In vivo* bioluminescent tomography using multi-spectral and multi-perspective image data," in *Biomedical Optics 2006 Technical Digest*, Optical Society of America, Washington D.C., TuG4 (2006).
18. G. Alexandrakis, F. R. Rannou, and A. F. Chatziioannou, "Tomographic bioluminescence imaging by use of a combined optical-PET (OPET) system: a computer simulation feasibility study," *Phys. Med. Biol.* **50**, 4225–4241 (2005).
19. O. Coquoz, T. L. Troy, D. Jekic-McMullen, and B. W. Rice, "Determination of depth of *in vivo* bioluminescent signals using spectral imaging technique," *Proc. SPIE* **4967**, 37–45 (2003).
20. H. Dehghani, S. C. Davis, S. D. Jiang, B. W. Pogue, K. D. Paulsen, and M. S. Patterson, "Spectrally resolved bioluminescence optical tomography," *Opt. Lett.* **31**, 365–367 (2006).
21. A. J. Chaudhari, F. Darvas, J. R. Bading, R. A. Moats, P. S. Conti, D. J. Smith, S. R. Cherry, and R. M. Leahy, "Hyperspectral and multispectral bioluminescence optical tomography for small animal imaging," *Phys. Med. Biol.* **50**, 5421–5441 (2005).
22. A. Ishimaru, *Wave Propagation and Scattering in Random Media*, Academic Press, New York (1978).
23. J. Ripoll, V. Ntziachristos, R. Carminati, and M. Nieto-Vesperinas, "Kirchoff approximation for diffusive waves," *Phys. Rev. E* **64**, 051917 (2001).
24. M. Keijzer, W. M. Star, and P. R. M. Storchi, "Optical diffusion in layered media," *Appl. Opt.* **27**, 1820–1824 (1988).
25. A. Lagendijk, R. Vreeker, and P. DeVries, "Influence of internal reflection on diffusive transport in strongly scattering media," *Phys. Lett. A* **136**, 81–88 (1989).
26. J. X. Zhu, D. J. Pine, and D. A. Weitz, "Internal reflection of diffusive light in random media," *Phys. Rev. A* **44**, 3948–3959 (1991).
27. R. C. Haskell, L. O. Svaasand, T. Tsay, T. Feng, M. S. McAdams, and B. J. Tromberg, "Boundary conditions for the diffusion Eq. in radiative transfer," *J. Opt. Soc. Am. A* **11**, 2727–2741 (1994).
28. C. L. Lawson and R. J. Hanson, *Solving Least Squares Problems*, pp. 160–165, Prentice-Hall, Englewood Cliffs, NJ (1974).
29. A. Joshi, W. Bangerth, and E. M. Sevick-Muraca, "Adaptive finite element based tomography for fluorescence optical imaging in tissue," *Opt. Express* **12**, 5402–5417 (2004).
30. M. Takeda, H. Ina, and S. Kobayshi, "Fourier-transform method of fringe-pattern analysis for computer-based topography and interferometry," *J. Acoust. Soc. Am.* **72**, 156–160 (1982).
31. D. C. Ghiglia and M. D. Pritt, *Two-Dimensional Phase Unwrapping, Theory, Algorithms, and Software*, John Wiley and Sons, New York (1998).
32. M. L. Vernon, J. Frechette, Y. Painchaud, S. Caron, and P. Beaudry, "Fabrication and characterization of a solid polyurethane phantom for optical imaging through scattering media," *Appl. Opt.* **38**, 4247–4251 (1999).
33. S. A. Prahl, M. J. C. van Gemert, and A. J. Welch, "Determining the optical properties of turbid media by using the adding doubling method," *Appl. Opt.* **32**, 559–568 (1993).
34. J. W. Pickering, S. A. Prahl, N. van Wieringen, J. F. Beek, J. Sterenborg, and M. J. van Gemert, "Double integrating sphere system for measuring the optical properties of tissue," *Appl. Opt.* **32**, 339–410 (1993).
35. T. Troy, D. Jekic-McMullen, L. Sambucetti, and B. Rice, "Quantitative comparison of the sensitivity of detection of fluorescent and bioluminescent reporters in animal model," *Mol. Imaging* **3**, 9–23 (2004).
36. F. Bevilacqua, D. Piguet, P. Marquet, J. D. Gross, B. J. Tromberg, and C. Depeursinge, "In vivo local determination of tissue optical properties: applications to human brain," *Appl. Opt.* **38**, 4939–4950 (1999).